REPORT DOCUMENTATION PAGE

1. REPORT DATE *(DD-MM-YYYY)*	2. REPORT TYPE	3. DATES COVERED *(From - To)*
November 2012	Technical Paper	November 2012-January 2013

4. TITLE AND SUBTITLE

Computational Investigation of Combustion Dynamics in a Lean-Direct Injection Gas Turbine Combustor

5a. CONTRACT NUMBER
In-House

5b. GRANT NUMBER

5c. PROGRAM ELEMENT NUMBER

6. AUTHOR(S)
Yoon, C., Gejji, R., Anderson, W. and Sankaran, V.

5d. PROJECT NUMBER

5e. TASK NUMBER

5f. WORK UNIT NUMBER
5K-61RZS

7. PERFORMING ORGANIZATION NAME(S) AND ADDRESS(ES)

Air Force Research Laboratory (AFMC)
AFRL/RQR
5 Pollux Drive.
Edwards AFB CA 93524-7048

8. PERFORMING ORGANIZATION REPORT NO.

9. SPONSORING / MONITORING AGENCY NAME(S) AND ADDRESS(ES)
Air Force Research Laboratory (AFMC)
AFRL/RQR
5 Pollux Drive
Edwards AFB CA 93524-7048

10. SPONSOR/MONITOR'S ACRONYM(S)

11. SPONSOR/MONITOR'S REPORT NUMBER(S)

AFRL-RZ-ED-TP-2012-478

12. DISTRIBUTION / AVAILABILITY STATEMENT
Distribution A: Approved for Public Release; Distribution Unlimited. PA#13088

13. SUPPLEMENTARY NOTES
Conference paper for the 51st AIAA Aerospace Sciences Meeting, Dallas, Texas, 7-10 January 2013.

14. ABSTRACT

Combustion dynamics is investigated using an integrated computational/experimental approach for a laboratory-scale, single-element lean direct injection model combustor in which self-excited pressure oscillations are produced. The present study focuses on physics based computational simulations that fully describe the turbulence, spray, combustion and acoustics phenomena in the combustion chamber. Baseline three-dimensional results at an equivalence ratio = 0.47 confirm the self-excitation of acoustic modes in the chamber and also indicate the presence of precessing vortex core instabilities. Preliminary comparisons of the pressure oscillations with experimental measurements are also presented. Further, the effects of multi-dimensionality, equivalence ratio and secondary atomization are computationally investigated. In contrast to the 3D simulations, two-dimensional models capture the pressure oscillations with reasonably similar amplitudes, but show inherent limitations in describing the vortex breakdown process. Pressure oscillations are also shown to be intensified when the equivalence ratio is increased and damped when the secondary atomization effects are included.

15. SUBJECT TERMS

16. SECURITY CLASSIFICATION OF:			17. LIMITATION OF ABSTRACT	18. NUMBER OF PAGES	19a. NAME OF RESPONSIBLE PERSON Venkateswaran Sankaran
a. REPORT	b. ABSTRACT	c. THIS PAGE	SAR	20	19b. TELEPHONE NO *(include area code)* 661-525-5534
Unclassified	Unclassified	Unclassified			

Computational Investigation of Combustion Dynamics in a Lean-Direct Injection Gas Turbine Combustor

Changjin Yoon[1], Rohan Gejji[2] and William E. Anderson[3]
Purdue University, West Lafayette, IN 47907

and

Venkateswaran Sankaran[4]
Air Force Research Laboratory, Edwards AFB, CA, 93524

Combustion dynamics is investigated using an integrated computational/experimental approach for a laboratory-scale, single-element lean direct injection model combustor in which self-excited pressure oscillations are produced. The present study focuses on physics-based computational simulations that fully describe the turbulence, spray, combustion and acoustics phenomena in the combustion chamber. Baseline three-dimensional results at an equivalence ratio = 0.47 confirm the self-excitation of acoustic modes in the chamber and also indicate the presence of precessing vortex core instabilities. Preliminary comparisons of the pressure oscillations with experimental measurements are also presented. Further, the effects of multi-dimensionality, equivalence ratio and secondary atomization are computationally investigated. In contrast to the 3D simulations, two-dimensional models capture the pressure oscillations with reasonably similar amplitudes, but show inherent limitations in describing the vortex breakdown process. Pressure oscillations are also shown to be intensified when the equivalence ratio is increased and damped when the secondary atomization effects are included.

I. Introduction

Combustion dynamics present significant challenges to the development of gas turbine engines. Several undersirable engine operational issues such as NOx/CO emissions, flame stability, etc. are closely related with this phenomenon. Combustion dynamics may arise from the coupled interactions between the unsteady heat release, chamber acoustics, turbulence, spray and hydrodynamic instabilities at the compressor and turbine interfaces. The presence of such the multi-variable inputs to the combustor makes the understanding of combustion dynamics extremely complex and difficult.

The Lean Direct Injection (LDI) method is a well-known design concept wherein the liquid fuel is directly injected into the flame zone and is mixed rapidly with the air in the shortest possible distance. Compared with conventional designs, the LDI method provides improved NOx performance and eliminates the issues encountered in the Lean Prevaporized Premixed (LPP) method such as auto-ignition and flash-back. However, as the push to aggressively lower NOx emission continues, LDI combustors are increasingly susceptible to combustion instabilities. In fact, as the equivalence ratio approaches lean operating conditions, the chemical kinetics and the flame surface can become more responsive to the acoustic fluctuations in the combustor. Moreover, there are also no natural damping mechanisms of the acoustic waves generated by the large vortices produced by the orifices.

---

[1] Postdoctoral Researcher, School of Aeronautics and Astronautics, and Member AIAA.
[2] Graduate Researh Assistant, School of Aeronautics and Astronautics, and Student Member AIAA.
[3] Professor, School of Aeronautics and Astronautics, and AIAA Associate Fellow.
[4] Senior Scientist, Propulsion Directorate, AIAA Senior Member.

"Approved for public release; distribution is unlimited."

Longitudinal combustion instabilities are the main concern in LDI combustors. According to Cohen et al.'s experimental study[1], longitudinal model pressure oscillations are reported to be within 3% of the mean chamber pressure. They have also successfully demonstrated longitudinal mode combustion instabilities with similar pressure oscillation magnitudes in laboratory-scale LDI engines. Yi and Santavicca's experimental study[2] focused on flame spectra in the LDI combustor, which they observed to be very similar to those observed in lean premixed gaseous combustion. They further used correlations from chemiluminescence data to parametrically represent the effects of the instantaneous air consumption rate, heat release rate and equivalence ratio on the combustion instabilities. Their results at atmospheric conditions indicate that the instabilities grow from 4.48% to 9.93% when the equivalence ratio is decreased from 0.34 to 0.32 for a half-wave mode combustor. Palies et al.'s study[3] of premixed confined swirling flames also provides meaningful insight on flame response. Their results indicate that the unsteady heat release occurred in the 0-400 Hz range which corresponds generally to the longitudinal mode frequencies. Through analytical and experimental studies, they further conclude that the flame undergoes axial acoustic and azimuthal velocity fluctuations because of the vorticity wave generation from the swirler.

Combustion instabilities in LDI combustors are fundamentally different from those encountered in dump combustors. When the flow expands through the venturi, axial decay of the tangential velocity and the radial pressure gradient induce recirculation bubbles near the centerline. These bubbles can be unstable, and result in development of the so-called Precessing Vortex Core (PVC) instabilities. PVC instabilities are frequently found in the swirling combustor flows.[4] Patel and Menon's computational study[5] of spray combustion flowfields predicted the formation of PVC instabilities in the LDI combustor. Syred and Beer[6] suggest that the PVC frequency linearly increases with the mass flow rate. Liang and Maxworthy[7] confirmed that the PVC instabilities can happen even at moderate Reynolds number, such as Re = 1000. Such flow instabilities are significant because they can represent an important mechanism that feeds the unsteady heat release and thereby contributes to the occurrence of combustion instabilities.

The present study is aimed at computationally predicting self-excited combustion instabilities in a laboratory-scale LDI combustor. The experimental results are used to validate the capabilities of the computational model. For the baseline case, gas-phase, spray, chemistry and acoustic characteristics are investigated. Next, the combustion dynamics is parametrically examined in terms of the equivalence ratio, and the secondary atomization. Both 2D and 3D simulations are used to carry out these parametric assessments.

II. Laboratory-Scale LDI Combustor

A. Experimental Set-Up

The experimental arrangement of the laboratory scale LDI fed combustor shown in Figure 1. The single element combustor design is based on axial mode combustion dynamics with a fundamental frequency of 400 Hz. The combustor is designed in a modular configuration so that various lengths of the air plenum section and combustion chamber section can be tested. The modular design of the combustor is essential to map the effect of combustor configurations on the combustion dynamics and also to tune the required frequencies and pressure amplitude fluctuations in the combustor. The appropriate major dimensions of the modular sections of the combustor are determined based on an analytical 1-D model in the Linearized Euler Equation (LEE) solver.[8]
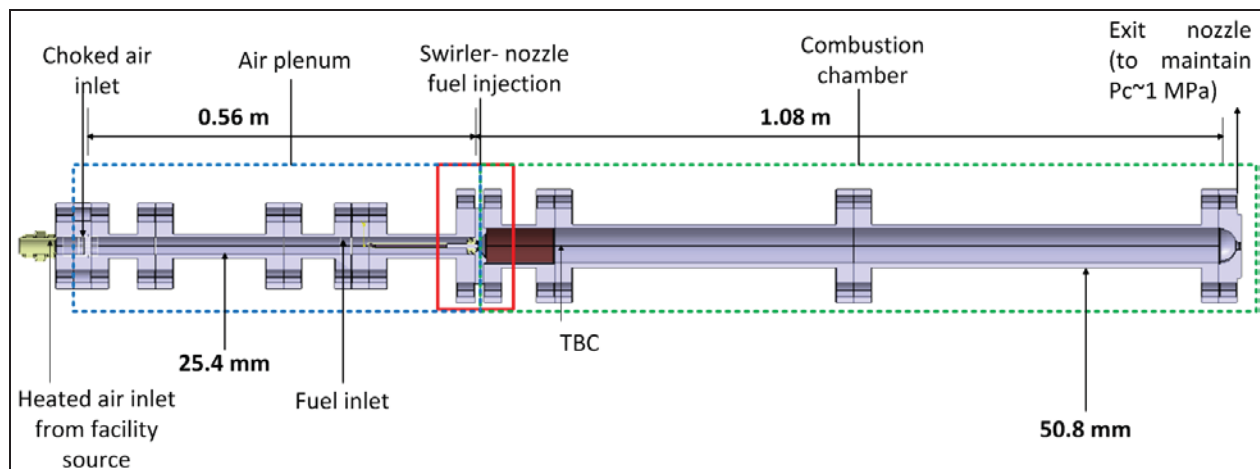

Figure 1 Schematic diagram of the experimental arrangement of the LDI combustor

The combustor has been designed to operate with Jet-A as the fuel and heated air as the oxidizer. The overall length of the air plenum section of the combustor is 0.56 m and the length of the combustion chamber is 1.08 m. Heated air is provided to the experiment at temperatures as much as 900 K from a choked inlet section made up of multiple slots. The choked multiple slots provide minimum flow disturbances downstream into the air plenum section compared to other geometries that are viable for computational analysis. A detailed computational description showing the effects of inlet geometry on air flow in the air plenum section is presented in a later section.

The heated air passes through a helical vane swirler (60° vane angle) before being accelerated into the combustion chamber via a subsonic converging diverging venturi. The swirler has six helical vanes and is fixed to the fuel injector. The fuel is injected into the combustor using a low flow number (1.32) pressure swirl atomizer. The fuel enters the combustor at the throat of the venturi in its nominal location. The fuel injector position can be varied upstream or downstream of the throat of the venturi. The inlet section of the combustion chamber has a thermal barrier coating applied to it to avoid heat loss through the walls and provides a near-adiabatic boundary condition. This allows for better comparison with computational results where an adiabatic wall boundary condition is typically employed. The combustion chamber has a choked exit orifice that sets the chamber pressure in the combustor. Choked inlet and exit orifices on the combustor also help set a closed acoustic boundary condition.

The design envelope for the experiments is tabulated in Table 1 below. The experimental results and comparison with the computational simulation results are presented in later sections of the paper.

Table 1 Summary of design envelope and nominal operation parameters

Fuel	-	Jet-A/ JP8
Oxidizer	-	Air
Inlet Air Temperature	(K)	750 (nominal)
Equivalence Ratio	-	0.6 (nominal)
Frequency	(Hz)	400
Inlet Boundary Condition	-	Constant mass inflow from choked orifice
Exit Boundary Condition	-	Choked nozzle
Diameter of combustor	(mm)	50.8 mm (2.0 inches)
Diameter of air plenum section	(mm)	25.4 mm (1.0 inch)

B. Computational Mesh and Boundary Conditions

In the simulations, all surfaces except for the inlet and exit planes are treated as no-slip and adiabatic walls. The inlet plane is located at the top left end of Figure 1 and the air flow enters radially through the inlet using a constant mass flow rate condition. At the exit nozzle, the outlet condition is imposed by specifying the back pressure.

A hexahedral unstructured mesh system is used for the full geometry as shown in Figure 1 and butterfly meshing is used for the circular cross-sections. A total of 3.7 million cells are constructed for the present simulations. According to our grid refinement studies, coarser meshes of one to two million cells were found to be incapable of properly resolving the acoustic oscillations.
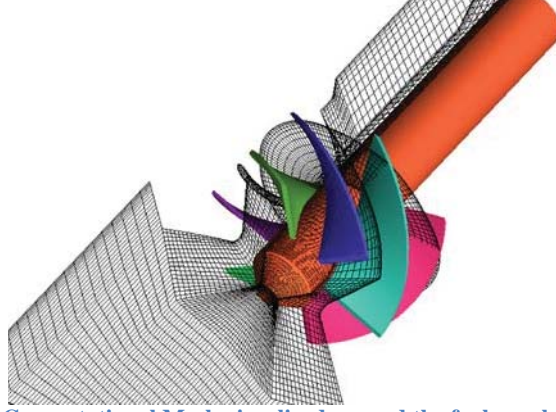
Figure 2 Computational Mesh visualized around the fuel nozzle and swirler

III. Computational Model

A. Eulerian Phase Equations

The computational platform for the present simulations is our in-house code, GEMS (General Equation and Mesh Solver).[9-12] GEMS is a fully unstructured, density-based finite volume solver with a second-order numerical scheme and an implicit, dual time procedure for time-accuracy. The capabilities of the code for capturing combustion dynamics and estimating instabilities have been successfully demonstrated for rocket engines combustors.[13, 14] GEMS solves the Navier-Stokes equations in Detached Eddy Simulation (DES) mode along the continuity, energy and species equation described below.

$$\frac{\partial Q}{\partial t} + \nabla \cdot \left(F - F_v \right) = S \tag{1}$$

where the conservative variables, Q, inviscid and viscous flux vectors, F and F_v, and source term vector, S, are given by

$$Q = \begin{pmatrix} \rho \\ \rho \mathbf{Y} \\ \rho \mathbf{V} \\ \rho h^0 - p \\ \rho \mathbf{K} \end{pmatrix}, \quad F = \begin{pmatrix} \rho \mathbf{V}^T \\ \rho \mathbf{Y} \mathbf{V}^T \\ \rho \mathbf{V} \mathbf{V}^T + p \bar{I} \\ \rho h^0 \mathbf{V}^T \\ \rho \mathbf{K} \mathbf{V}^T \end{pmatrix}, \quad F_v = \begin{pmatrix} 0 \\ \rho D \nabla \mathbf{Y} \\ \bar{\tau} \\ \bar{\tau} \cdot \mathbf{V} - q \\ \mu_K \nabla \mathbf{K} \end{pmatrix} \quad \text{and} \quad S = \begin{pmatrix} 0 \\ \dot{\omega} \\ 0 \\ 0 \\ s_K \end{pmatrix} + S_L \tag{2}$$

The quantities; ρ, $\mathbf{V}$ and p represent the density, velocity vector and pressure, respectively; h^0 is the stagnation enthalpy and $\mathbf{Y}$ is a species mass fraction vector; $\mathbf{K}$ represents the turbulence variable vector which includes turbulence kinetic energy and specific dissipation, k and w; In the viscous flux, D is the molecular diffusion coefficient; τ is the stress tensor and q is the heat flux; w and s_K are the reaction rate and sources of the turbulence transport equations, respectively. A pseudo-time term expressed in terms of the primitive variables, $Q_p = \begin{bmatrix} p & \mathbf{Y} & \mathbf{V} & T & \mathbf{K} \end{bmatrix}^T$ and a preconditioning matrix, Γ, is added to Eq. (1), so that the equation becomes:

$$\Gamma \frac{\partial Q_p}{\partial \tau} + \frac{\partial Q}{\partial \tau} + \nabla \cdot \left(F - F_v \right) = 0 \tag{3}$$

The matrix, Γ, is chosen to control the artificial dissipation in the spatial discretization and the convergence of the pseudo-time iterations. The preconditioning matrix, Γ, in the pseudo time term in Eq. (3), is defined by starting from the Jacobian of the conservative variables with respect to the primitive variables, $\partial Q / \partial Q_p$, as shown below:

$$\Gamma = \begin{pmatrix} \rho_p{}' & \rho_\mathbf{Y} & 0 & \rho_T & 0 \\ \rho_p{}'\mathbf{Y} & \rho_\mathbf{Y}\mathbf{Y} + \rho & 0 & \rho_T\mathbf{Y}^T & 0 \\ \rho_p{}'\mathbf{V} & \rho_\mathbf{Y}\mathbf{V} & \rho\bar{\mathbf{I}} & \rho_T\mathbf{V}^T & 0 \\ \rho_p{}'h^0 - (1 - \rho h_p) & \rho_\mathbf{Y}h^0 + \rho h_\mathbf{Y} & \rho\mathbf{V}^T & \rho_T h^0 + \rho h_T & 0 \\ \rho_p{}'\mathbf{K} & \rho_\mathbf{Y}\mathbf{K} & 0 & \rho_T\mathbf{K} & \rho \end{pmatrix} \tag{4}$$

where the primed quantities refer to scaled values that control the accuracy and efficiency of the pseudo-time iterations.

The flux formulation for a generalized upwind finite volume approach can be interpreted as the average of the fluxes on either side of the cell interfaces augmented by an artificial dissipation term,

$$\tilde{F} = \frac{1}{2}(F_L + F_R) - \frac{1}{2}|A|(Q_R - Q_L) = \frac{1}{2}(F_L + F_R) - \frac{1}{2}\Gamma|\Gamma^{-1}A_p|(Q_{pR} - Q_{pL}) \tag{5}$$

where the subscripts R and L represent values on the right and left side of the cell face. The numerical procedure uses a second-order approximate Riemann solver to evaluate the spatial fluxes at cell faces. Second-order temporal accuracy is achieved by means of an implicit dual time procedure that eliminates factorization and linearization errors.

B. Turbulence Model

The present simulations describe the large-scale, time-dependent turbulence motion by means of a Detached Eddy Simulation (DES) model.[15-18] DES is a hybrid RANS/LES approach which combines the RANS model in the attached boundary layers with the LES method in the large separation and wake regions.

A DES model can be obtained from any RANS model and our DES formulation uses the k-omega two-equation model with the appropriate modifications.[18] Switching from RANS to LES mode is enabled by appropriately reducing the dissipation term in turbulent kinetic energy transport equations. Specifically, the DES model replaces the length scale with the minimum of the length scale defined in turbulence model for RANS and maximum spacing of the local grid as:

$$l_{DES} = \min\left(l_{k-\omega}, C_{DES}\delta\right) \tag{6}$$

where $\delta = \max(\Delta x, \Delta y, \Delta z)$ represents the maximum grid spacing in any direction and C_{DES} is a model constant and set equal to 0.78 as recommended by Travin et al.; $l_{k-\omega}$ is the length scale of Wilcox's k-w two equation model for the turbulence closure in RANS and it is defined as

$$l_{k-\omega} = \frac{k^{1/2}}{\beta^*\omega} \tag{7}$$

where β^* is a model constant. This definition of the length scale by Eq. (6) ensures that the RANS mode is utilized near the wall surface in which the high grid aspect ratio is typically expected. Finally, the dissipation term in the transport equation of the turbulence kinetic energy is replaced by

$$\beta^*\rho kw = \frac{\rho k^{3/2}}{l_{DES}} \tag{8}$$

This modification ensures that the resulting sub-grid model reduces to a Smagorinky-like model at equilibrium.

C. Combustion Model

The six chemical species considered for the propellant combination in the LDI combustor are $C_{12}H_{23}$, O_2, CO_2, H_2O, CO and N_2. They are solved directly and turbulence transport in the species equations is modeled using the classical gradient model with a constant Schmidt number. Laminar finite rate chemistry model is used to evaluate the reaction rate. Although flamelets and transported-FMDF models are popular in unsteady LES simulations, their capabilities for predicting combustion/acoustic interaction problems are not well-established, particularly, because these models are based upon constant pressure flame assumptions.

We consider the fuel as $C_{12}H_{23}$ to approximate the experimental Jet-A fuel. A simplified two-step, five species global reduced mechanism has been incorporated in the present study.[19]

$$2C_{12}H_{23} + 35O_2 \longrightarrow 24CO + 23H_2O$$

$$\text{and} \quad 2\mathbf{CO} + \mathbf{O_2} \longleftrightarrow 2\mathbf{CO_2}$$
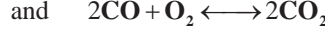
The kinetics of the two-step global reactions are represented by an Arrhenius function of the form as:

$$\dot{\omega} = AT^n \left(-E_a / R_u T \right) \left[\mathbf{X_A} \right]^a \left[\mathbf{X_B} \right]^b \tag{9}$$

where w is the production rate, A is the pre-exponential constant, E_a is the activation energy, and n, a and b are exponents, respectively. For the first $C_{12}H_{23}$ oxidation step, the production rate is expressed with constants as $2.643 \times 10^9 \exp(-1.5108 \times 10^4/T)[C_{12}H_{23}]^{0.25}[O_2]^{1.5}$ (Kmol/m^3-sec). And it is expressed as $2.2387 \times 10^{12} \exp(-2.0143 \times 10^4/T)[CO][O_2]^{0.25}[H_2O]^{0.5}$ (Kmol/m^3-sec) for the forward CO oxidation reaction in the second step, and $5.0 \times 10^8 \exp(-2.0143 \times 10^4/T)[CO_2]$ (Kmol/m^3-sec) for the reverse CO dissociation reaction.

D. Lagrangian Phase Equations

The Lagrangian formulation for the liquid particle motion is expressed as a set of ordinary differential equations for the Lagrangian solution variables, Q_L, as:

$$\frac{dQ_L}{dt} = \frac{d}{dt} \begin{pmatrix} \mathbf{X} \\ \mathbf{U} \\ T_l \\ m_l \\ r \end{pmatrix} = \begin{pmatrix} \mathbf{U} \\ F_D \left(\mathbf{V} - \mathbf{U} \right) \\ \dot{m}_v \left[c_p \left(T_g - T_l \right) - L_v \right] / m_l C_l \\ -\dot{m}_v \\ -\dot{m}_v / \left(4\pi r^2 \right) \end{pmatrix} \tag{10}$$

where $\mathbf{X}$, $\mathbf{U}$, T_l, m_l and r are the components of the Largrangian solution vector and these variables represent the position and velocity vector, temperature, mass and radius for the liquid particle, respectively. The first and second rows represent the motion of particle drops in which only the drag is considered as an external force. In the source of second row, F_D is a drag parameter accounting for $F_D = \frac{3}{8} \frac{C_D}{r} \frac{\rho_g}{\rho_l} |\mathbf{U} - \mathbf{V}|$ in which $\mathbf{V}$ is the carrier gas velocity vector and the drag coefficient follows Putnam's formulation[20] based on the spherical drop assumption.

$$C_D = \begin{cases} 0.44 & \text{Re} < 1000 \\ \dfrac{24}{\text{Re}} \left(1 + \dfrac{1}{6} \text{Re}^{2/3} \right) & \text{Re} > 1000 \end{cases} \tag{11}$$

where Reynolds number, Re, is defined as $\dfrac{\rho_g d}{\mu_g} |\mathbf{U} - \mathbf{V}|$. The third row in Eq. (10) represents the energy equation for the liquid particle. This equation assumes the uniform temperature inside the liquid particle. The source term consist of the net sensible enthalpy transfer, $c_p \left(T_g - T_l \right)$, and the latent heat of vaporization, L_v, and $m_l C_l$ represents the heat capacity of the liquid particle. The fourth row accounts for mass balance during vaporization. The corresponding source term is the vaporization rate, $\dot{m}_v$, which is evaluated by means of the classical D^2-law:

$$\dot{m}_v = -2\pi r \rho_g D_s \text{Sh} \ln \left(1 + B_M \right) \tag{12}$$

where D_s is a diffusion coefficient at the liquid surface and Sh is a Sherwood number; B$_M$ is the Spalding mass transfer number[21] given by

$$B_M = \frac{Y_{F,s} - Y_{F,\infty}}{1 - Y_{F,s}} \tag{13}$$

where Y_F is the fuel species, subscripts s and ∞ indicate the surface and far field, respectively. The last row accounts for the particle radius reduction due to vaporization.

A set of Lagrangian phase equations, Eq. (10), is integrated explicitly and the Lagrangian time step is determined by the consideration of time scales like the particle lifetime, atomization initiation time and Eulerian time step, etc. All other physical properties of liquid particle except for Q_L are updated every time step as well.

E. Injection and Secondary Atomization Model

The fuel spray is described by the injection of a series of discrete liquid parcel which contains a certain number of drops. This parcel (or blob) is the particle solved by the Lagrangian phase equations. Note that the parcel is not an actual drop, but rather a cloud that contains a number of drops. The present simulation defines the spray cone by the

angle, origin of the ray and injected plane. Within the spray cone and defined injection plane, the parcel is randomly located in the radial and azimuthal directions and injected at a given speed.

Secondary atomization is modeled by the Reitz's breakup model.[22, 23] According to Patel and Menon's study[5], this model exhibits better accuracy than other existing models in LDI combustor environments. The atomization process in the Reitz model is based on the Kelvin-Helmholtz instability phenomenon and the results of the linear stability analysis are directly used in determining the important parameters in the atomization process. For easier use of the linear stability analysis results, the maximum growth rate, Ω, and corresponding wavelength, Λ, of the Kelvin-Helmholtz instability mode are expressed by curve-fits in terms of nondimensional numbers as:

$$\Omega \left[\frac{\rho_l a^3}{\sigma} \right]^{0.5} = \frac{\left(0.34 + 0.38 \mathrm{We_g}^2\right)}{\left(1 + \mathrm{Oh}\right)\left(1 + 1.4 \mathrm{Ta}^{0.6}\right)} \tag{14}$$

$$\frac{\Lambda}{a} = 9.02 \frac{\left(1 + 0.45 \mathrm{Oh}^{0.5}\right)\left(1 + 0.4 \mathrm{Ta}^{0.7}\right)}{\left(1 + 0.87 \mathrm{We_g}^{1.67}\right)^{0.6}} \tag{15}$$

where $\mathrm{We_g}$ is the weber number for the gas phase, $\mathrm{We_g} = \frac{\rho |\mathbf{U} - \mathbf{V}|^2 d}{\sigma}$, Oh is the Ohnesorge number, $\mathrm{Oh} = \nu_1 \sqrt{\frac{\rho_l}{\sigma a}}$ and Ta is the Taylor parameter, $\mathrm{Ta} = \mathrm{Oh}\sqrt{\mathrm{We_g}}$. The liquid breakup is modeled by adding new child parcels and their size is determined by

$$r = \begin{cases} B_0 \Lambda & \left(B_0 \Lambda \le a\right) \\ \min \begin{bmatrix} \left(3\pi a^2 |\mathbf{U} - \mathbf{V}| / 2\Omega\right)^{0.33} \\ \left(3a^2 \Lambda / 4\right)^{0.33} \end{bmatrix} & \left(B_0 \Lambda > a, \text{ one time only}\right) \end{cases} \tag{16}$$

where B_0 is a model constant and set equal to 0.61. Simultaneously, the parent drop size is reduced by

$$\frac{da}{dt} = -\frac{(a - r)}{\tau} \tag{17}$$

where τ is a time constant and determined from

$$\tau = 3.726 B_1 a / \Lambda \Omega \tag{18}$$

Child parcels are released when the stripped mass removed from the parent parcel exceeds a few percentages of the average injected parcel mass. Newly formed parcels have the random velocity direction in a confined cone angle defined by

$$\tan(\theta / 2) = A_1 \Lambda \Omega / U \tag{19}$$

where $A_1 = 0.188$. In addition, while the parent parcel reduces, its mass is preserved by controlling the drop numbers contained in a parcel as $Na^3 = N_0 a_0^3$.

F. Eulerian-Lagrangian Coupling

Eulerian-Lagrangian coupling is through the source term vector, S, in Eq. (2). Mass, chemical species, momentum and energy transfer from the Lagrangian phase are specified as source terms in the Eulerian phase.

$$S_L = \frac{d}{dt} \begin{pmatrix} \rho \\ \rho \mathbf{Y} \\ \rho \mathbf{V} \\ \rho h^0 - p \\ \rho \mathbf{K} \end{pmatrix} = \begin{pmatrix} \sum_N n \dot{m}_v \\ \sum_N n \dot{m}_v \\ \sum_N n \left(\dot{m}_v \mathbf{U} - m_l \dot{\mathbf{U}}\right) \\ \sum_N n \left(\dot{m}_v h_v - \dot{m}_v Q_d\right) \\ 0 \end{pmatrix} \tag{20}$$

where the subscripts N and n represent the number of parcels and the number of drops in an individual parcel respectively.

IV. Investigation of Inlet Geometry Effects

Dynamic flow response for several inlet configurations is investigated to aid in the design of an inlet configuration that introduces little or no downstream unsteady effects. Axisymmetric non-reacting flow simulations

are used in these studies for fast turn-around of the parametric studies with different inlet configurations. In order to meet the desired chamber pressure under the given mass flow rate, the exit nozzle size is reduced. In all other respects, the computational domain remains unchanged from the target experimental design.

It is anticipated that a choked inlet condition would be well-suited for isolating the waves traveling upstream from the combustion chamber and thereby maintaining a constant mass flow rate through the device. However, there is concern that flow instabilities due to vortex shedding downstream of the choked throat may influence the thermoacoustic mode in the combustion chamber. Therefore, this study is targeted at investigating the fluid dynamics characteristics of four candidate inlet geometry designs, all of which are choked: a nozzle with a strong shock, nozzle with a subsonic diffuser, nozzle with a weak shock and a slotted inlet design. In the first three cases, the degree of expansion in the divergent section was controlled to see how the fluid dynamics is affected by the design. In the last instance, the inlet consisted of multiple choked slots with a sudden expansion to the dimensions of the oxidizer post.

According to the computational investigations, it is found that the choked slot inlet exhibits the most stable flow pattern among four inlet geometries. Table 2 summarizes these results and quotes the observed frequency in the combustion chamber that results from the vortex shedding downstream of the choked inflow. Figure 3 shows the flowfield immediately downstream of the choked slots and it is evident that the flowfield quickly stabilizes and looks almost steady by the time it reaches the end of the oxidizer post. In contrast, all the nozzle cases showed periodic vortex shedding in the air plenum (not shown), and natural oscillations are observed in the wall pressure history and power spectrum density (PSD) as shown in Figure 4 for the choked nozzle with weak shock flow condition. In this case, large amplitude wall pressure oscillations are detected in the pressure history and the dominant frequency and the subharmonics are highlighted. The natural frequency (6000 Hz) here corresponds to a Strouhal number of 0.4-0.6 which is located at the range of the hydrodynamics instabilities usually found in similarly designed injectors. Slight changes in the natural frequencies (9000 Hz) are observed for the choked nozzle with strong shock condition because of the flow interaction with the shock train downstream of the nozzle. For the choked slot case given in Figure 5, no distinct frequencies are observed indicating that the combustor flow is not strongly influenced by the fluid dynamics of the inlet. For this reason, the choked slot inlet geometry is selected for further study both in the experiments and in the computations.
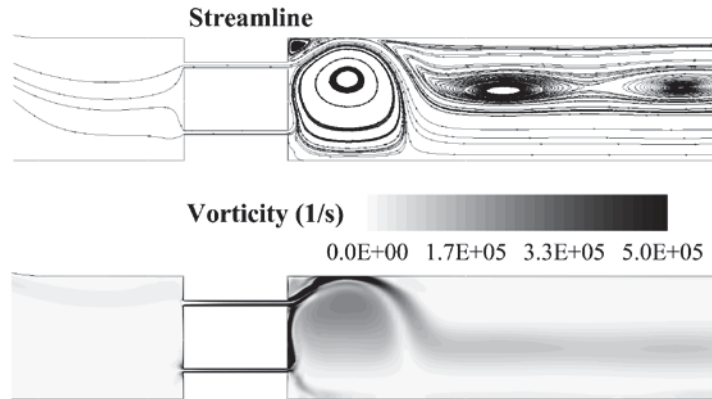

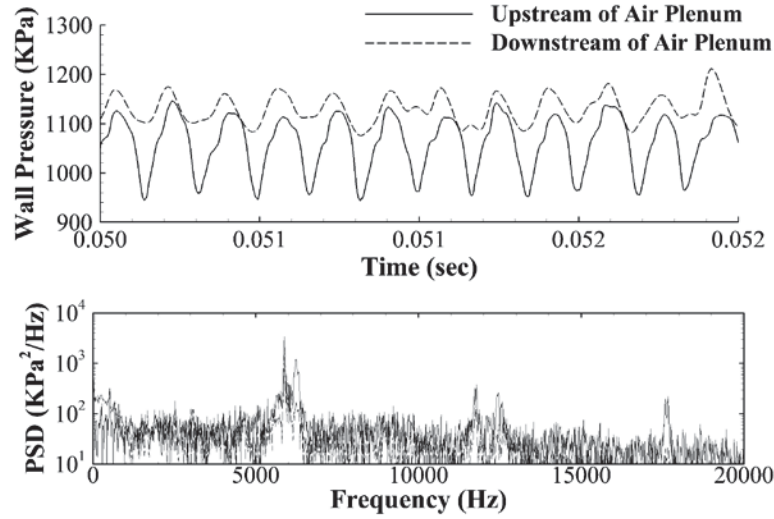**Figure 3 Choked slot flows from the non-reacting flow simulation**

Figure 4 Wall pressure history and PSD results for choked nozzle with a weak shock
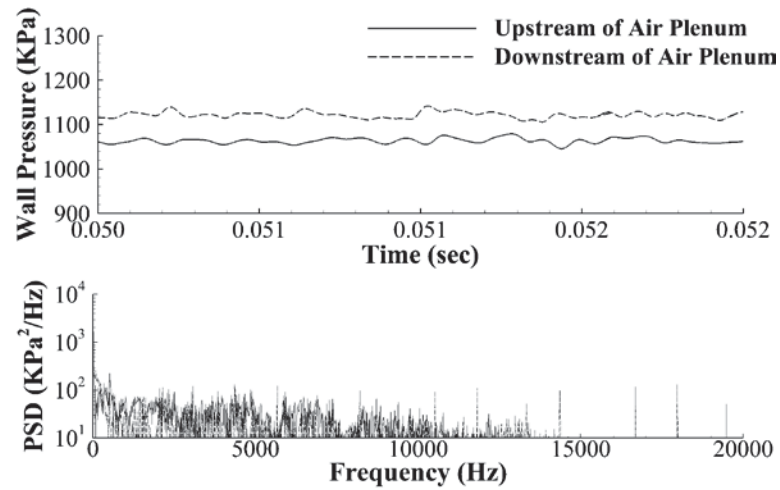

Figure 5 Wall pressure history and PSD results for choked slot

Table 2 Summary of the inlet study

Case	Unsteadiness	Frequency (Hz)	Flow Features
1: Choked nozzle with a strong shock	Yes	9000	- Oscillations with a shock train - Filled with lower pressure than the chamber pressure by the supersonic flow until the middle of air plenum
2: Choked nozzle with a subsonic diffuser	Yes	6000	- Typical hydrodynamic instabilities with large fluctuations of the mass flow rate and pressure
3: Choked nozzle with a weak shock	Yes	6000	- Typical hydrodynamic instabilities with small fluctuations of the mass flow rate and pressure
4: Choked slot	No	-	- Large recirculation zone anchored right after slots - No unsteady motions in the air plenum

V. Investigation of Self-Excited Combustion Instabilities

A series of simulations are conducted for a total 8 cases to assess the effects of equivalence ratio, atomization and multi-dimensionality. Two different equivalence ratios, 0.47 and 0.73, with and without the secondary atomization effects are considered for 2D and 3D simulations, respectively. First, we take a look at the flow characteristics for the baseline case, which is a 3D simulation at $\Phi = 0.47$ including the effects of secondary atomization. We then examine the combustion dynamics and the resulting self-excited instabilities as a function of the above parameters.

A. Flow, Spray, Reaction and Acoustic Characteristics of Baseline Case

Particular attention of the flow characteristics is paid to the region around the lean direct injection element where large-scale vortical structures are typically present. The swirl number is used to characterize swirling flow and is defined as the ratio of the axial flux of angular momentum to the axial flux of axial momentum as:

$$S = \frac{\int \rho r V_\theta (\mathbf{V} \cdot d\mathbf{A})}{r \int \rho V_x (\mathbf{V} \cdot d\mathbf{A})} \tag{21}$$

It is customary to approximate the swirl number based on uniform flow and geometric assumptions as[24]:

$$S_a = \frac{R_2^2 + R_1^2}{2R_2^2} \tan(\theta_m) \tag{22}$$

The corresponding swirl number, S_a, in Eq. (22) is 0.57 with the present LDI element dimensions ($R_1 = 0.34$ in, $R_2 = 0.8725$ in, theta $= 60°$). However, we note that this approximation exhibits a significant difference from the swirl number of 0.82, which is obtained by using Eq. (21) on the time-averaged result. Here, the time-averaged flow at the axial location of the fuel nozzle exit is used for the swirl number calculation.
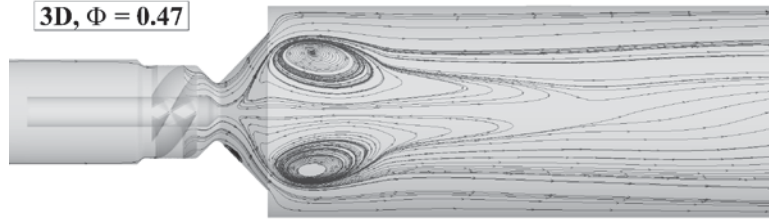

Figure 6 Time-averaged streamline at the axial-cut surface

The time-averaged streamlines in an axial-cut surface of the combustor is shown in Figure 3 and reveals the presence of twin counter-rotating nearly-axisymmetric stationary vortex pair at the combustor head. Reverse flow is evident between the twin vortices and the stagnation point is located in the center of the diverging section of the venture between the fuel nozzle and combustor head. The overall flow structure agrees well with the experimental visualization by Liang and Maxworthy[7]. They report that such a flow pattern is susceptible to self-excited oscillations beyond a swirl number of 0.88 and, as noted above, the present case is operating close to this value.

The oscillating motion of the vortex pair can be detected in the time-series data and is associated with the presence of a precessing vortex core (PVC). The characteristic frequency of the PVC is observed to be around 3100 Hz. Figure 4 shows the iso-surface contours of the Q-criterion as a series of snapshots in time over a single period of vortex motion. The PVC is observed to start from the fuel injector exit and continue to spiral in the swirling direction until the combustor head. The time evolution of PVC is also associated with an unsteady heat release pattern in the azimuthal direction as seen in Figure 5. It is evident that the predicted maximum heat release occurs at the location of PVC tail in Figure 4, which indicates that the vortex core leads to enhanced mixing and combustion.
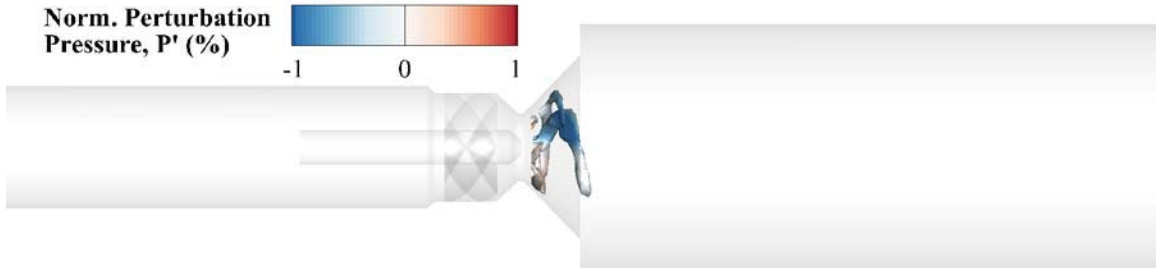
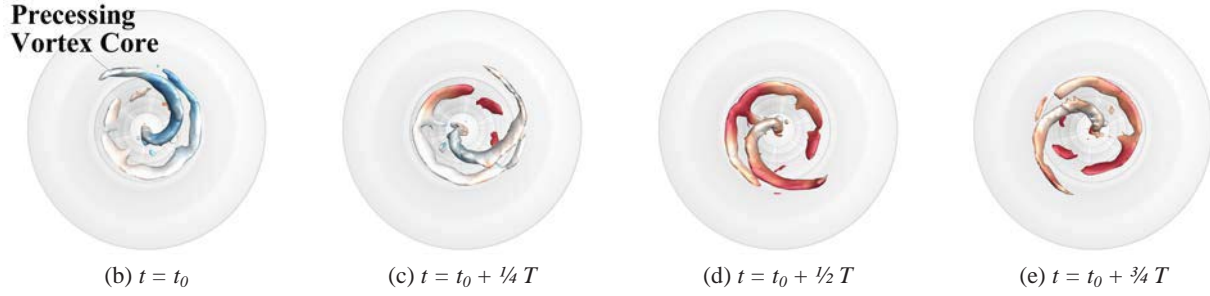(a) Longitudinal view around the fuel nozzle at $t = t_0$

(b) $t = t_0$ (c) $t = t_0 + \frac{1}{4} T$ (d) $t = t_0 + \frac{1}{2} T$ (e) $t = t_0 + \frac{3}{4} T$

Figure 7 Time evolution of Precessing Vortex Core Instabilities for a single period (f_{PVC} = 3100 Hz) visualized by Q-criterion iso-surface and colored by normalized perturbation pressure
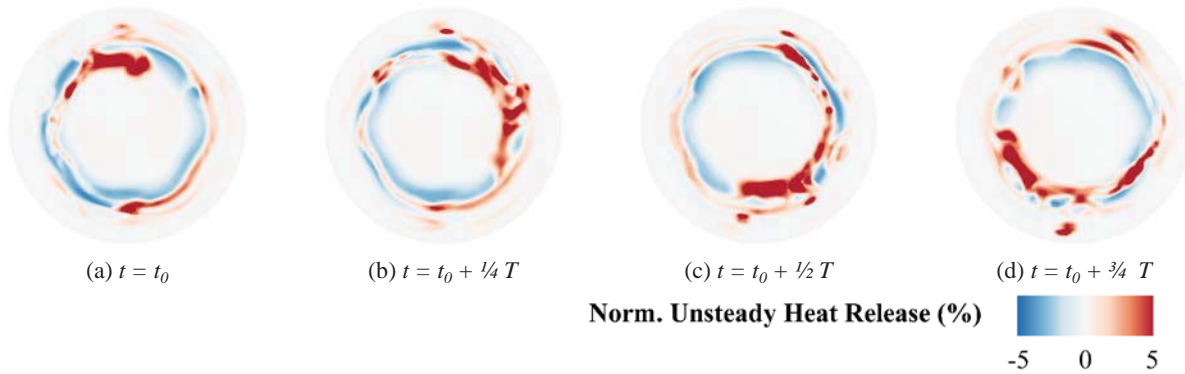

(a) $t = t_0$ (b) $t = t_0 + \frac{1}{4} T$ (c) $t = t_0 + \frac{1}{2} T$ (d) $t = t_0 + \frac{3}{4} T$

Norm. Unsteady Heat Release (%)

-5   0   5

Figure 8 Time evolution of heat release at the cross-section of combustor head for a single PVC mode

Atomization, vaporization, mixing and reaction rapidly occur in the swirling shear layer. The injected spray drops encounter strong aerodynamic forces due to the swirling gas flow, which in turn causes the secondary breakup due to Kelvin-Helmholtz instability. The resulting smaller drops are readily heated and vaporized near the reaction zone. The fast vaporization combined with the mixing with the swirling air results in initiation of combustion. Simulation results indicate all these process take place in the venturi diverging section. Figure 6 shows the resulting temperature distribution along with the spray and streamlines. The flowfield shows the presence of the large three-dimensional vortex structure and the spray drops are seen to be fully consumed at the combustor head. Hot temperature mixture in the centerline of the combustor results from the strong chemical reaction in the venturi diverging section, while the unburned air flows around the combustion zone keeping the combustor wall relatively cool.
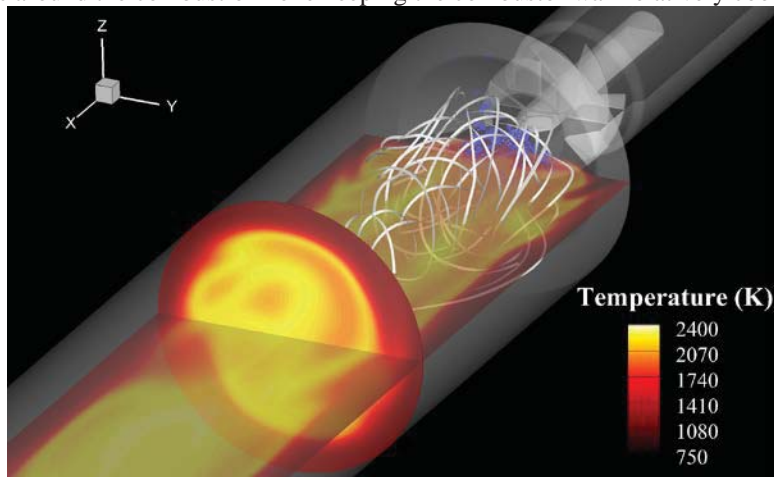

Figure 9 Instantaneous temperature distribution with spray and streamlines

Self-excited combustion-driven instabilities are the result of the unsteady heat release being in-phase with the acoustic pressure perturbations in the geometry. At $\Phi = 0.47$, the present 3D results of the acoustic waves and the unsteady heat release are shown in Figure 7 and Figure 8 respectively. The dominant frequency from the power spectral density (PSD) analysis is located at the 2L mode frequency of 800 Hz, and the corresponding pressure amplitude at the combustor head is 3%. The exact mechanism of coupling of the heat release with the acoustics is difficult to ascertain from these figures and more careful assessment of the spray distribution and gas-phase mixing is necessary to reach definitive conclusions.

Norm. Perturbation Pressure, P' (%)

-1   0   1
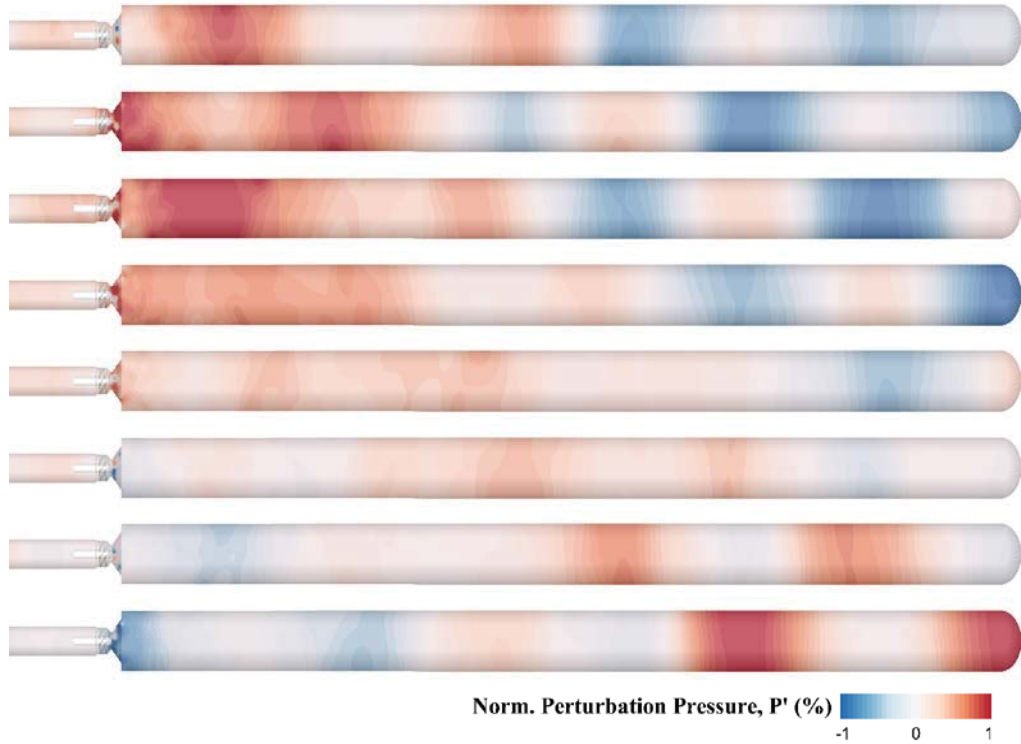
Figure 10 Combustion-driven acoustic waves traveling in the combustor during a 2L mode period (f_{2L} = 763 Hz)

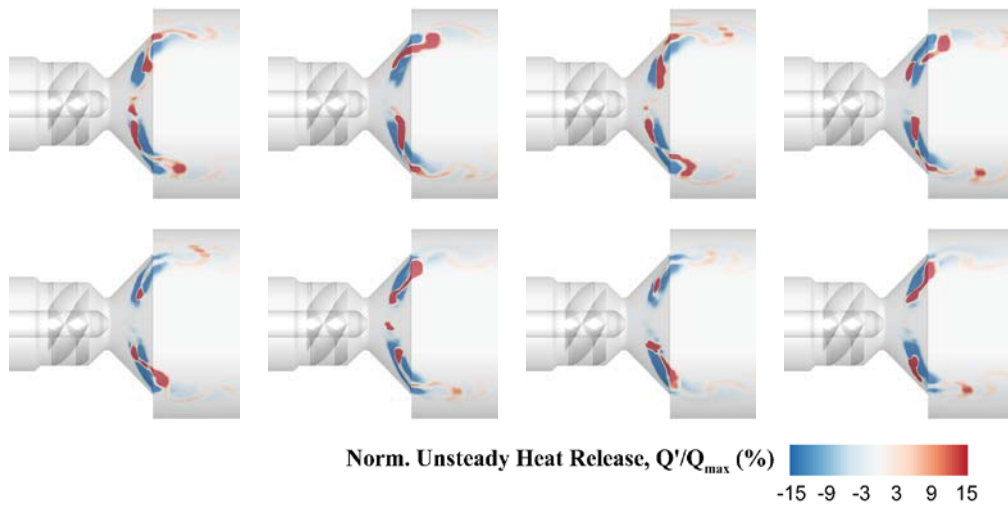Norm. Unsteady Heat Release, Q'/Q_{max} (%)

-15 -9 -3   3   9 15

Figure 11 Unsteady Heat Release Pattern for a 2L mode period

Pressure measurements on the wall at the head end of the combustion chamber are compared between the experiment and simulations. It is important to note slight differences between the experiment and simulations before

comparing the results between them. The simulation considers the fuel injector to be at the throat of the subsonic venturi while in the experiment is 2.6 mm upstream of the throat. Secondly, the equivalence ratio measured during the experiment was 0.49 instead of 0.47. The air temperature was maintained at 750 K for both the simulation and the experiment.

The PSD results from computational and experimental results are presented in Figs. 9 and 10, respectively. Longitudinal acoustic peaks are distinctly found approximately every 400 Hz from both results. Some discrepancies are found in the dominant oscillation mode. The experimental result indicates the strongest peak at the 4L mode, whereas the computation estimates the dominant peak at the 2L mode. Insufficient descriptions of fuel spray modeling as well as differences in the location of the fuel injector between simulations and experiment are thought to be few of the critical factors leading to inaccuracies in estimation of the pressure oscillations. The fuel spray arbitrarily defined in the present study is currently being tuned based on detailed spray diagnostics data and will be presented in future publications.
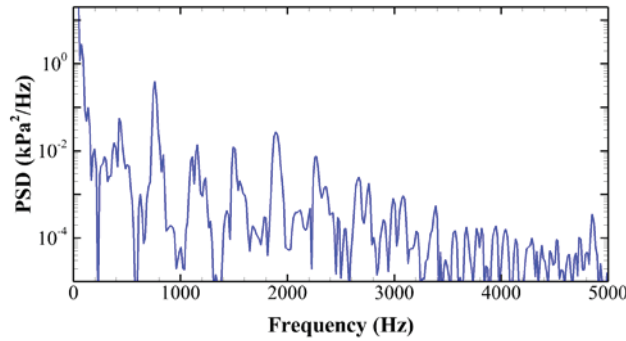

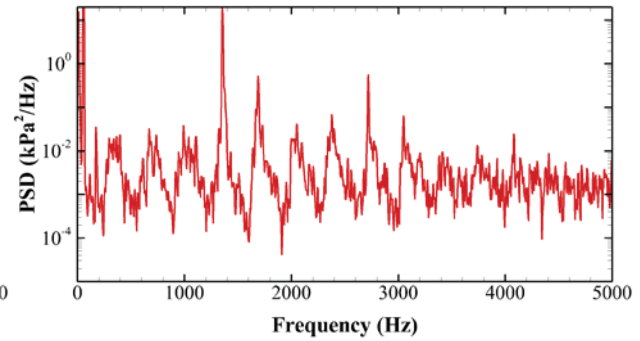Figure 12 PSD at the combustor head wall from the simulation results

Figure 13 PSD at the combustor head wall from the experimental results

B. Combustion Dynamics

1. Comparisons between 2D and 3D simulations

In the present study, 2D axisymmetric simulations are used as a preliminary diagnostic tool for analyzing trends in the LDI combustor. While the 2D model has inherent limitations for capturing the full multi-dimensional description of the turbulent reacting spray flowfield, it is still an attractive option that provides quick insight into the combustion dynamics. A notable feature of our 2D model is that the swirling source is introduced at the location that corresponds to the swirler vane section and the magnitude of the source term is tuned to match the exit flow angle to the swirl vane angle.

A significant difference in the flow pattern of the 2D computations is caused by the insufficient description of vortex breakdown process. Unlike the 3D simulation in which a stationary twin vortex pair is formed, a series of vortices behind the twin vortex pair are observed as seen in Figure 11. The secondary vortices are created due to the absence of the physical vortex breakdown process and this discrepancy in turn influences the flow field in the upstream section of the combustor. Moreover, the swirling momentum generated in the swirl vane section is sustained over the whole combustor length because of inadequate damping in the two-dimensional case.
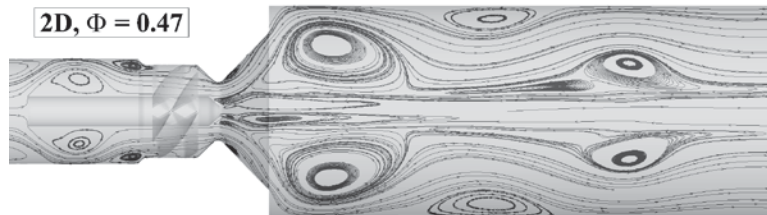

Figure 14 Time-averaged streamline in 2D simulation

A consequence of the strong swirling momentum in the 2D case is that the injected drops at the edge of the spray cone are quickly atomized and vaporized, while the dense spray is distributed near the centerline. Also, the stronger fuel momentum due to the dense spray drops moves the stagnation point further the downstream and further influences the flowfield near the centerline. As a result, rich fuel distribution and low temperatures at the centerline

are observed in the 2D case as seen in Figure 17. Moreover, the 2D simulations cannot predict the PVC phenomena and therefore the dynamics response related to these frequencies are not represented.
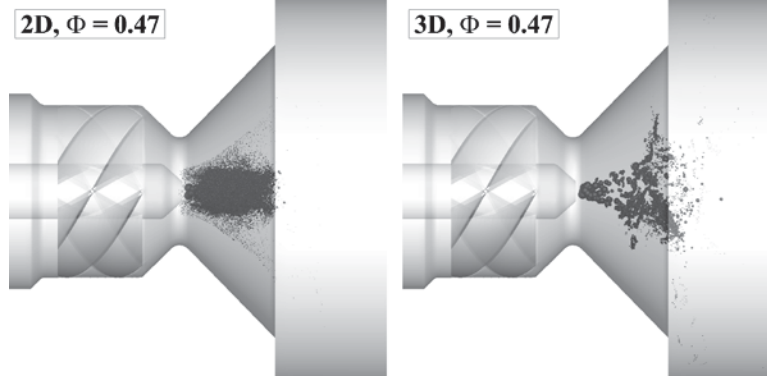

Figure 15 Spray Flow Pattern in 2D and 3D results

Figure 18 shows the wall pressure PSD results for both the 2D and 3D simulations. The self-excited oscillations at the combustor head wall are well captured in both simulations with reasonably similar amplitudes (about 7%). However, the dominant frequency in the 2D simulation is found to be the 1L mode (400 Hz) whereas the 3D results show the 2L mode to be dominant. This discrepancy is probably related to the differences in the heat release pattern and the temperature distribution. Moreover, in the 2-D case, the results are noisier at the high frequency range, f > 3000 Hz, which can be attributed to lack of vortex damping mechanisms as noted earlier.
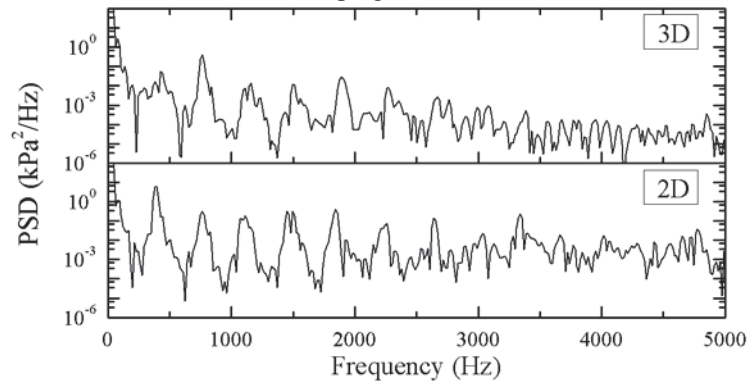

Figure 16 Wall Pressure PSD at the combustor head in 2D and 3D simulations

2. Effects of Equivalence Ratio
The equivalence ratio is controlled by varying the fuel mass flow rate, while keeping the air mass flow rate fixed. Two equivalence ratios, 0.47 and 0.73, are considered here. The vaporized fuel is distributed within a conical shape in the diverging section of the venturi and is fully consumed prior to reaching the combustor head. For $\Phi = 0.73$, a larger amount of oxygen is consumed at the combustor head than for $\Phi = 0.47$, resulting in a wider area of high temperature in the combustor as seen in Figure 14.
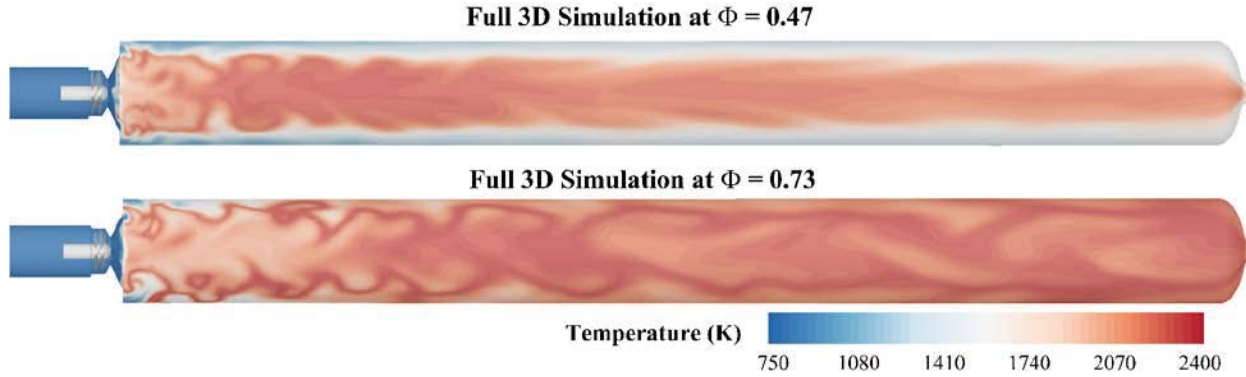
Figure 17 Instantaneous temperature distribution in terms of equivalence ratio

In the wall pressure PSD results shown in Figure 10, more distinct and stronger pressure peaks are found for the $\Phi = 0.73$ case. The dominant frequency at $\Phi = 0.73$ is the 1L mode at 427 Hz mode unlike for the $\Phi = 0.47$ where the dominant mode is the 2L mode. The level of pressure amplitude is approximately 11%. A series of subharmonic frequencies follow with weaker strengths. Moreover, another strong pressure peak is observed at the 1T mode frequency of 10 KHz, especially for the $\Phi = 0.73$ case. In fact, the strength of the 1T mode is comparable with that of the 1L mode for $\Phi = 0.73$, whereas the 1T mode for $\Phi = 0.47$ is relatively weak. The stronger intensity of the pressure oscillations for the $\Phi = 0.73$ case may be attributed to the stronger heat release and more uniform temperature distribution noted earlier.
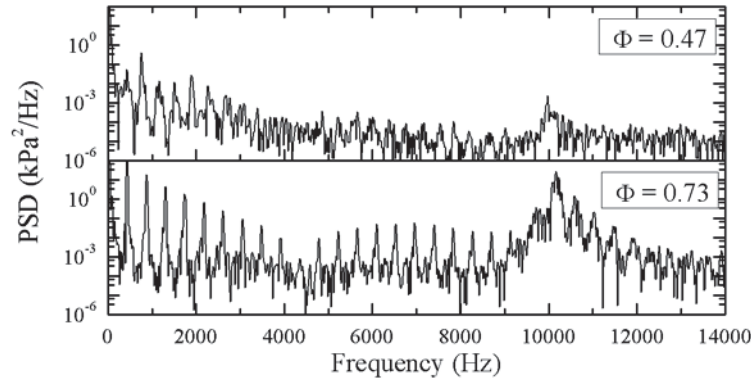

Figure 18 Wall Pressure PSD at the combustor head in terms of the equivalence ratio

3. Secondary Atomization Effects

The present study assumes that the initial injected drops originate from the primary breakup and then undergo secondary atomization as a result of Kelvin-Helmholtz instabilities. In order to isolate the effects of secondary atomization effects, we also consider the simulation results for a log-normal size distribution of the initial injected drops without any secondary atomization model.

Figure 16 shows a very different spray distribution when the secondary atomization model is included compared to when it is not. Firstly, the secondary atomization model leads to a larger number of fine drops. The mean parcel number in the combustor is 2,500 without secondary atomization, whereas it is 11,000 with secondary atomization. Secondly, the secondary atomization effects appear to cause a stronger interaction with surrounding carrier gas flow. In this case, the swirling shear layer, the secondary atomization rapidly breaks up the original spray and the broken drops are transmitted to the reaction zone by the carrier gas. On the other hand, in the simulations without secondary atomization, the spray cone shape remains relatively undisturbed by the surrounding gas-phase flow.
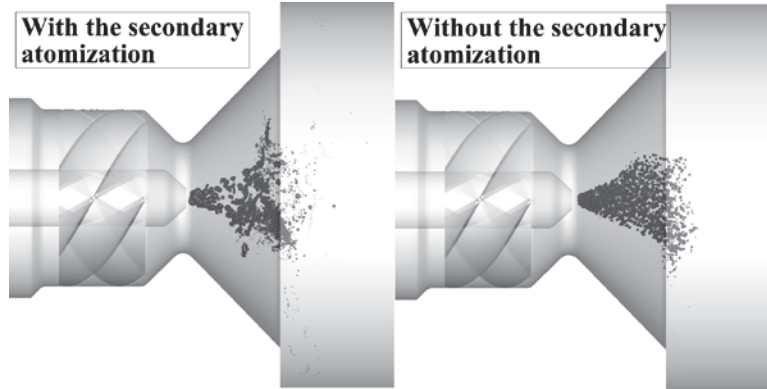
American Institute of Aeronautics and Astronautics

Figure 19 Spray Flow Pattern with respect to the secondary atomization

Figure 17 and Figure 18 show the time-averaged spray mass and size distributions, which provide information about the life cycle of spray drops. Most of the spray drops are seen to be distributed within the diverging section of the venturi (X < 0.012 m) and consumed at the combustor head. Also, the time-averaged spray mass distribution at the injector exit indicates similar qualitative trends with or without secondary atomization. However, approximately twice the number of spray drops survive in the case without secondary atomization, implying that the secondary atomization leads to more rapid vaporization. It is interesting that Figure 13 shows similar drop size distribution for the two cases except for the strong oscillatory aspect in the absence of secondary atomization. These peaks correspond to the initial drop sizes determined by the log-normal distribution and can be regarded as an artificial effect. It is noteworthy that the size distribution in the simulation with secondary atomization follows the mean of the case without secondary atomization.
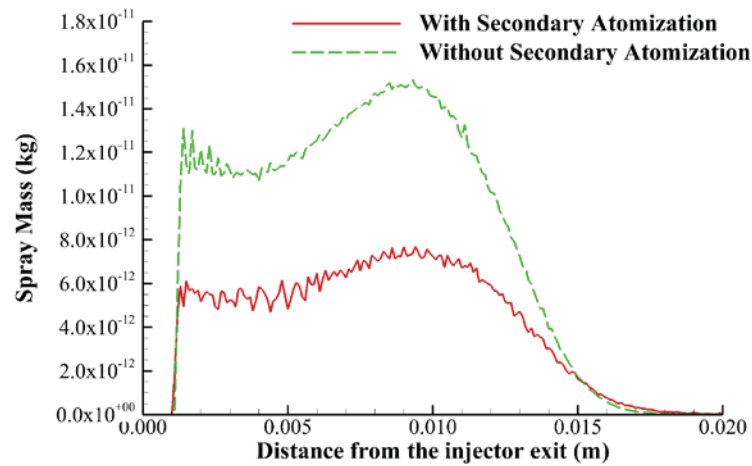

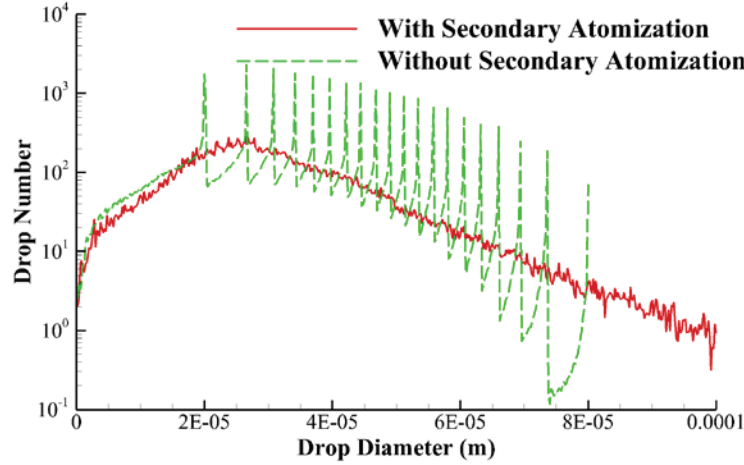**Figure 20 Time-averaged spray drop distribution from the injector exit**

American Institute of Aeronautics and Astronautics

Figure 21 Time-averaged size distribution

Another noteworthy result is the spray response due to the acoustic waves shown in Figure 19. When the high pressure acoustic wave reaches the combustor head-end (Figure 19a), the spray flow is suppressed by the pressure rise and secondary atomization is observed to be prevalent around the region of the fuel nozzle. A larger number of fine drops are then observed in the venturi. As the pressure decreases at the head-end, the spray recovers its original conical shape as seen in Figure 19(b). This spray response can be attributed to the effects of drag on the spray motion and the effects of the high Weber number on secondary atomization. When the pressure is high, the aerodynamic effects of the drop motions grows stronger due to the larger density magnitudes. The spray drops encounter the larger drag force, which results in the shorter penetration and suppression of the spray. Also, the high Weber number environments due to the increased density aid the rapid secondary atomization of the Kelvin-Helmholtz breakup mode.
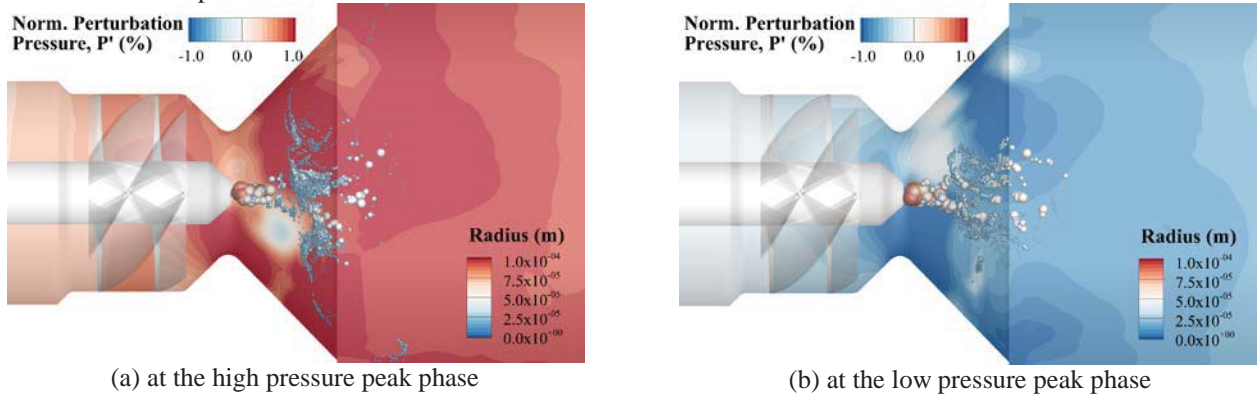

(a) at the high pressure peak phase   (b) at the low pressure peak phase

Figure 22 Spray response to the self-excited thermoacoustic waves

Self-excited pressure oscillations at the combustor head wall are investigated for both conditions: without and with atomization. Stronger and more distinct pressure peaks are found in the simulation without the secondary atomization model. We further observe that the dominant frequency changes from the 1L to the 2L mode due to the atomization effects. Exact reasons for the mode change are difficult to ascertain for sure without additional computations. However, we speculate that the ordered, well-distributed spray cone distribution in the no-atomization case lead to simpler physics and a response mechanism that is dominated by vaporization. In the case with secondary atomization, the response of the spray distribution and break-up in addition to the vaporization leads to a much more complex coupling scenario.
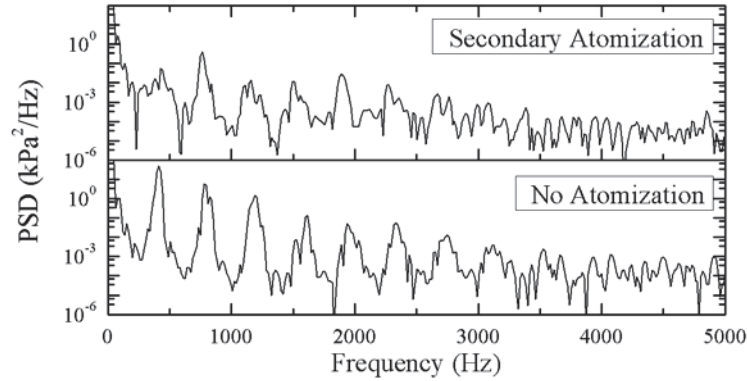
Figure 23 Wall Pressure PSD at the combustor head in terms of the atomization effect

VI. Summary

The present study predicts self-excited combustion instabilities in a laboratory LDI combustor. The simulations successfully capture the coupled diverse physics: fluid dynamics, sprays, combustion and acoustics and provides the first steps towards understanding the driving mechanism of the instabilities. The simulation results for the baseline case, $\Phi = 0.47$, indicates that PVC instabilities in the azimuthal direction occur at f = 3100 Hz and their evolution is directly associated with the heat release pattern. Also, the spray is rapidly atomized, vaporized and mixed with the air flow and combustion processes occur mainly in the venturi and combustor head. The longitudinal-mode pressure oscillations are found to be about 3% amplitude magnitude which is close to the oscillation levels in the experimental LDI combustor. For the baseline equivalence ratio, the dominant frequency is found to be the 2L mode at f = 763 Hz.

Combustion dynamics are investigated parametrically in terms of the 2D vs. 3D, varying the equivalence ratio, and with and without secondary atomization model effects. As the equivalence ratio approaches the stoichiometric ratio, longitudinal oscillations grow stronger and the frequency characteristics change. The 1L mode is now observed to be the dominant frequency and the 1T mode is also apparent at f = 10 KHz with an amplitude that is comparable to that of the 1L mode. The presence of secondary atomization is observed to cause the spray drops to interact with flows and promotes strong vaporization in the combustor head. Also, the spray is seen to interact with the acoustic waves in the chamber. Suppression of the spray and strong atomization is observed when the pressure is high at the combustor head-end. Moreover, the inclusion of secondary atomization effects leads to mitigation of the self-excited pressure oscillations, implying that the atomization can play a role in damping the acoustic waves.

Future studies will focus on careful validation of the computational model with available experimental data. Additional enhancements of the fuel-spray are also planned, in particular, to represent the primary atomization effects of the injector more accurately. Further calculations and diagnostics will also be carried out to investigate the underlying driving mechanisms that promote the self-excited instabilities. In this regard, POD (Proper Orthogonal Decomposition) and DMD (Dynamic Mode Decomposition) techniques are being investigated to better characterize the pressure oscillations, spray dynamics and the combustion heat release.

Acknowledgments

Reference

[1]   Cohen et al., "Longitudinal Mode Aeroengine Combustion Instability: Model and Experiment," NASA TM-2000-210067, NASA Glenn Research Center, 2000.

[2]   T. Yi and D. A. Santavicca, "Forced Flame Response of Turbulent Liquid-Fueled Lean-Direct-Injection Combustion to Fuel Modulations," *Journal of Propulsion and Power*, Vol. 25, No. 6, 2009, pp. 1259—1271.

[3]   P. Palies et al., "The Combined Dynamics of Swirler and Turbulent Premixed Swirling Flames," *Combustion and Flame*, Vol. 157, No. 9, 2010, pp. 1698—1717.

   [4]   N. Syred, "A Review of Oscillation Mechanisms and the Role of the Precessing Vortex Core (PVC) in Swirl Combustion Systems," *Progress in Energy and Combustion Science*, Vol. 32, No. 2, 2006, pp. 93—161.

   [5]   N. Patel and S. Menon, "Simulation of Spray-Turbulence-Flame Interactions in a Lean Direct Injection Combustor," *Combustion and Flame*, Vol. 153, No. 1—2, 2008, pp. 228—257.

   [6]   N. Syred and J. M. Beer, "Combustion in Swirling Flows: a Review," *Combustion and Flame*, Vol. 23, 1974, pp. 143—201.

   [7]   H. Liang and T. Maxworthy, "An Experimental Investigation of Swirling Jets," *Journal of Fluid Mechanics*, Vol. 525, 2005, pp. 115—159.

   [8]   Y. Yu et al., "Effects of Mean Flow, Entropy Waves, and Boundary Conditions on Longitudinal Combustion Instability," *Combustion Science and Technology*, Vol. 182, No. 7, 2010, pp. 739—776.

   [9]   Li, D., Xia, G., Sankaran, V., Merkle, C. L., "Computational Framework for Complex Fluids Applications," *3rd International Conference on Computational Fluid Dynamics*, Toronto, Canada, July 12-16, 2004.

   [10]   Xia, G., Sankaran, V., Li, D., and Merkle, C.L., "Modeling of Turbulent Mixing Layer Dynamics in Ultra-High Pressure Flows", *36th AIAA Fluid Dynamics Conference and Exhibit*, San Francisco, CA, June 05-08, 2006, AIAA 2006-3729.

   [11]   Lian, C., Xia, G. and Merkle, C. Solution-Limited Time Stepping to Enhance Reliability in CFD Applications. Journal of Computational Physics, Vol. 228, 2009, pp. 4836-4857.

   [12]   Lian, C., Xia, G. and Merkle, C. Impact of Source Terms on Reliability of CFD Algorithms. *The 19th AIAA Computational Fluid Dynamics*, San Antonio, TX, June 22-25, 2009.

   [13]   Smith, R., Xia, G., Anderson, W.A., and Merkle, C.L. (2010), "Computational Simulations of the Effect of Back-Step Height on Non-Premixed Combustion Instability", *AIAA Journal*, V. 48, No. 9, pp1857-1868, September, 2010.

   [14]   Smith, R., Ellis, M., Xia, G., Sankaran, V., Anderson, W. and Merkle, C.L., „Computational Investigation of Acoustics and Instabilities in a Longitudinal-Mode Rocket Combustor," *AIAA Journal*, Vol. 46, No. 11, November 2008, pp. 2659-2673.

   [15]   D. Basu et al., DES, Hybrid RANS/LES and PANS Models for Unsteady Separated Turbulent Flow Simulations, *ASME 2005 Fluids Engineering Division Summer Meeting, Houston*, TX, 2005, pp.683—688.

   [16]   F. R. Menter et al., A Scale-Adaptive Simulation Model using Two-Equation Models, 43rd AIAA Aerospace Sciences Meeting and Exhibit, 2005, doi: 10.2514/6.2005-1095.

   [17]   R. A. Baurle et al., Hybrid Simulation Approach for Cavity Flows: Blending, Algorithm, and Boundary Treatment Issues, *AIAA J.*, Vol. 41, No. 8, 2003, pp. 1463—1480, doi: 10.2514/2.2129.

   [18]   A. Travin et al., "Physical and Numerical Upgrades in the Detached-Eddy Simulation of Complex Turbulent Flows," *Advances in LES of Complex Flow, Fluid Mechanics and Its Applications*, Vol. 65, 2004, pp. 239—254, doi: 10.1007/0-306-48383-1_16.

   [19]   C. K. Westbrook, F. L. Dryer, *Combustion Science and Technology*, Vol. 27, 1981, pp. 31—43.

   [20]   A. Putnam, "Integratable Form of Droplet Drag Coefficient," *American Rocket Society Journal*, Vol. 31, No. 10, 1961, pp.1467—1468.

   [21]   G. M. Faeth, "Evaporation and Combustion of Sprays," *Progress in Energy and Combustion Sciences*, Vol. 9, 1983, pp.1—76.

   [22]   Reitz, R., "Modeling Atomization Processes in High-Pressure Vaporizing Sprays, *Atomisation and Spray Technology*, Vol. 3, 1987, pp. 309-337.

   [23]   M. Patterson and R. Reitz, Modeling the Effects of Fuel Spray Characteristics on Diesel Engine Combustion and Emission, SAE 980131, 1998

   [24]   Fu, Y., "Aerodynamics and Combustion of Axial Swirlers," Ph. D. dissertation from the University of Cincinnati, 2008.